

**ARTICLE TYPE****Study of UV line and continuum variabilities in the Broadline Seyfert 1 Galaxy ESO 141–G55**Mayukh Pahari\*<sup>1</sup> | Veda Samhita<sup>2</sup> | Harikumar N.<sup>3</sup> | Anurag Baruah<sup>1</sup> | Vivek Shinde<sup>1</sup><sup>1</sup>Department of Physics, IIT Hyderabad, Kandi, Sangareddy, Telangana, India<sup>2</sup>Department of Electronics and Communications Engineering, Vasavi College of Engineering, Hyderabad, Telangana, India<sup>3</sup>Physics and Astronomy Department, NIT Rourkela, Odisha, India**Correspondence**

\*Mayukh Pahari; Email: mayukh@phy.iith.ac.in

**Present Address**

PH209, Department of Physics, IIT Hyderabad, Kandi, Sangareddy, Telangana, India

We present the results from a 3-year-long Ultraviolet monitoring campaign of the broad line Seyfert 1 galaxy ESO 141–G55 using International Ultraviolet Explorer (IUE). By modelling all individual, extinction-corrected UV spectra in 1150–1978 Å and 1850–3348 Å wavelength range, we have observed a significant variability in both UV continuum and line fluxes. Variabilities due to ionised UV lines like SiIV, CIV and HeII are delayed with respect to the UV continuum by  $2.92^{+0.54}_{-0.61}$ ,  $4.41^{+0.44}_{-0.54}$ ,  $4.11^{+0.35}_{-0.81}$  days, respectively. At a distance of  $\sim 0.004c$ , an outer accretion disc can be a possible site for the origin of UV lines.

**KEYWORDS:**

accretion, accretion disks, galaxies: Seyfert, galaxies: Active, black hole physics

**1 | INTRODUCTION**

Seyfert 1 galaxies are a subclass of Active galactic nuclei (AGN) characterised by bright, point-like nuclei and broad permitted emission lines in their optical spectra, indicating the presence of high-velocity gas close to the central supermassive black hole (Khachikian & Weedman, 1974; Osterbrock, 1981). These systems exhibit significant ultraviolet (UV) emission, which originates from the innermost regions of the accretion disk (Shakura & Sunyaev, 1973). The UV continuum in Seyfert 1s often shows variability on timescales ranging from days to months, which is thought to be driven by instabilities or changes in the accretion flow and is frequently accompanied by corresponding changes in broad emission lines from broad line regions (BLRs) such as Ly $\alpha$   $\lambda$ 1216, C IV  $\lambda$ 1549, and He II  $\lambda$ 1640 (Clavel et al., 1991; Koratkar & Gaskell, 1991).

One of the most effective tools for probing the inner disk, BLR structure of AGN is reverberation mapping (RM) (Blandford & McKee, 1982; Peterson, 1993), particularly in UV. RM exploits the intrinsic variability of the continuum source - often the accretion disk and measures the time delays between fluctuations in the continuum and the corresponding response in the broad emission lines produced by photoionized gas in

the BLR. For measurements of time lag, we apply classical cross-correlation methods (Edelson & Krolik, 1988; Peterson, 1993) which uses randomization techniques like flux randomization and random subset selections. This lag represents the mean light travel time from the accretion disk to the BLR, thereby providing an estimate of the BLRs average distance from the central source. The primary objective of this work is to investigate the location of BLR through lag measurements, particularly, distinguishing the boundary between the BLR and the outer accretion disk using UV reverberation measurements. An accretion disk surrounds the supermassive black hole (SMBH), and the optical and ultraviolet (UV) emission seen in the spectral energy distribution (SED) of an active galactic nucleus (AGN) is believed to arise from the disks thermal radiation. Early models typically assumed a temperature profile based on the classical prescription by Shakura and Sunyaev (1973). In such a scenario, high-energy radiation striking the disk enhances its intrinsic thermal emission, resulting in a wavelength-dependent time delay, denoted by  $\tau$ , between the incoming high-energy photons and the reprocessed UV/optical emission. This delay follows the relation:  $\tau \propto (M^2 \dot{m}_E)^{1/3} \lambda^\beta$ , where  $\beta = 4/3$ ,  $M$  is the black hole mass, and  $\dot{m}_E$  is the accretion rate expressed in Eddington units. Earlier investigations (Cackett, Horne, & Winkler, 2007; Collier & et al.,

1999) supported the case where  $\beta = 4/3$  using optical observations. Recent multiwavelength reverberation studies, such as Fausnaugh et al. (2016), have shown that the measured UV-optical interband lags in NGC 5548 are a factor of about three larger than predicted by standard thin-disk models, indicating the presence of an oversized accretion disk. Guo, Barth, and Wang (2022) further confirmed this discrepancy using high-cadence UV-optical monitoring of several Seyfert 1 galaxies, suggesting that temperature fluctuations and diffuse continuum emission could contribute to the observed lag excess. More recently, Cackett et al. (2023) reported similar results from the AGN STORM 2 campaign on Mrk 817, reinforcing the oversized-disk problem and highlighting the need to refine current accretion disk and reprocessing models.

On the other hand, located farther out from the accretion disk, at a distance of approximately 0.001-0.1 parsecs, typical for Seyferts, is the BLR, which is responsible for producing emission lines. The UV/optical continuum emitted by the accretion disk photoionizes the gas clouds within the BLR. Since these clouds reside deep within the gravitational potential of the black hole, their resulting emission lines are broadened to velocities of several thousand kilometres per second. Therefore, the site of the reprocessing region is difficult to probe given the complexity of the central region.

ESO 141-G55 is a nearby ( $z = 0.0371 \pm 0.0003$ ; Grupe and Mathur 2004; Vaucouleurs et al. 1991) broad-line Seyfert 1 galaxy (BLS1). It was initially identified as an X-ray-bright AGN by Elvis and et al. (1978) in the Ariel 5 survey and confirmed as a Seyfert 1 through optical spectroscopy by M. Ward and et al. (1978). The galaxy exhibits a blue stellar nucleus and prominent optical and UV emission lines (M. J. Ward, Penston, Blades, & Turtle, 1978), along with significant variability in both the UV continuum and emission lines over timescales of months (Chapman & et al., 1985; Gaskell & et al., 1981). Archival IUE spectra of ESO 141-G55 have shown strong intrinsic UV variability. For instance, the 140 nm flux doubled between June and October 1980, increasing from  $0.8 \times 10^{-15}$  to  $1.6 \times 10^{-15} \text{ J m}^{-2} \text{ s}^{-1} \text{ nm}^{-1}$  (Gaskell & et al., 1981). In the X-ray regime, observations with EXOSAT revealed a flat 0.1–10 keV power-law slope with  $\Gamma = 1.52^{+0.03}_{-0.06}$  (Turner & Pounds, 1989), while subsequent measurements with Einstein and ROSAT showed a steeper photon index, with ROSAT finding  $\Gamma = 2.39 \pm 0.09$ , suggesting a soft X-ray excess (Turner & et al., 1991, 1993). More recent observations using XMM-Newton revealed a complex X-ray spectrum that includes a smooth soft excess, a broad Fe  $K\alpha$  line, and a pronounced Compton reflection hump, but no significant warm absorber features - leading to its classification as a bare AGN (Porquet et al., 2024). This bare-line-of-sight nature makes ESO 141-G55 an ideal target for reverberation studies, as it offers a clear, relatively unobscured view into the inner accretion disk and BLR.

In this paper, the ultraviolet properties of ESO 141-G55 have been explored using data from the International Ultraviolet Explorer (IUE), which observed the source in both the short and long wavelength ranges, covering multiple epochs between 1978 and 1982. The observations and data reduction methods are presented in Section 2. Section 3 outlines the results obtained from the spectral analysis. In Section 4.1, we present the time lag analysis between the UV continuum and prominent emission lines. Section 5, discusses the origin of ultraviolet line emissions and investigates the structure and scale of the broad-line region. Finally, concluding remarks about this work are presented in Section 6.

## 2 | OBSERVATIONS AND DATA REDUCTION

Between June 14, 1979 and March 15, 1991, the International Ultraviolet Explorer (IUE) performed 53 low-resolution short and long-wavelength spectral observations in the wavelength range of 1150-1978 Å and 1850-3348 Å. The analysis procedure follows the methodology described in Wanders et al. (1997). Raw IUE images are processed using the TOMSIPS (Ayres, 1993) and NEWSIPS (Nichols, Garhart, De La Pena, & Levay, 1993) data reduction pipelines. In this study, we adopt the NEWSIPS-reduced spectra, as recommended by Wanders et al. (1997). The TOMSIPS reduction suffers from a nonlinear wavelength calibration error due to uncorrected long-term drifts in the wavelength scale. In contrast, the NEWSIPS pipeline provides spectra that agree well with HST data, without requiring additional corr- and long-wavelength ranges, spanning the NEWSIPS pipeline, a small wavelength shift of approximately 1-2 Å is introduced due to pointing errors associated with the large aperture (Wanders et al., 1997). To correct for this, an offset compensation is applied to align the sharp C IV line feature across all spectra to a common average wavelength. The calculated interstellar reddening is significant with  $E(B-V) = 0.111$ . The reddening correction is applied to each spectrum following Calzetti (1999):

$$F_{obs}(\lambda) = F_{actual}(\lambda) \times 10^{-0.4 \times k(\lambda) \times E(B-V)} \quad (1)$$

where  $k(\lambda) = -2.156 + \frac{1.509}{\lambda} - \frac{0.198}{\lambda^2} + \frac{0.011}{\lambda^3}$ . The de-reddened spectra is shown in Figure 1 and Figure 2. The vertical blue lines indicate the offset corrected C IV emission at 1550.77 Å and Ly $\alpha$  emission at 1215.67 Å respectively. The redshift observed from the C IV average peak is consistent with the spectroscopic red-shift of  $z = 0.0371$  of Vaucouleurs et al. (1991).

Table 1 lists the IUE observations of ESO 141-G55. Out of the 53 total observations, 8 do not have any prominent emission features, which are not suitable for this work. Therefore, we use 46 observations for further analysis.

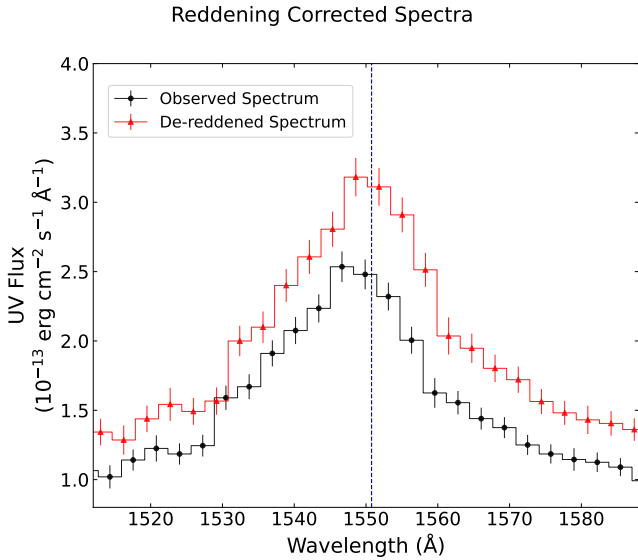


**FIGURE 1** Reddening-corrected UV spectra showing the observed (black) and de-reddened (red) flux distributions. There is significant increase in flux levels after the correction. The vertical blue dashed line marks the offset-corrected CIV emission feature at 1550.77 Å.

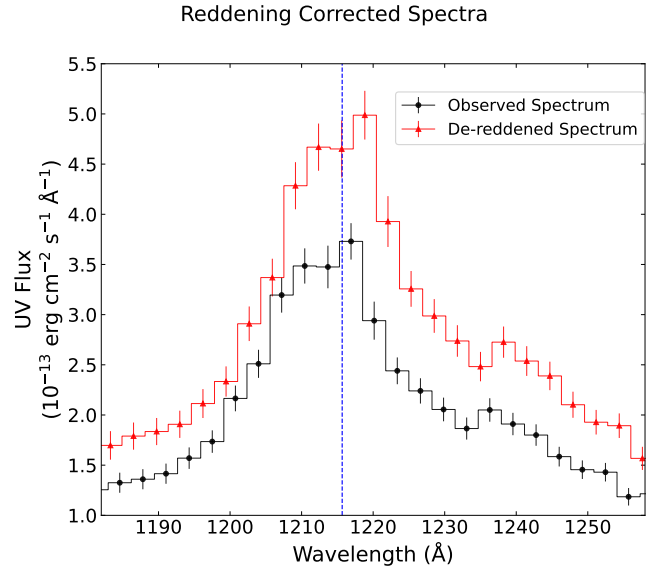


**FIGURE 2** Reddening-corrected UV spectra showing the observed (black) and de-reddened (red) flux distributions. There is significant increase in flux levels after the correction. The vertical blue dashed line marks the offset-corrected Ly $\alpha$  emission feature at 1215.67 Å.

### 3 | UV SPECTRAL ANALYSIS AND RESULTS

The IUE ultraviolet spectra exhibit significant variability in both line and continuum flux levels. An example of such variations is presented in Figure 3, where the flux observed on 5 June 1980 at 20:56:49 is notably different than that recorded on 2 October 1980 at 19:58:00.

To study the flux variability, we model light curves at different wavelengths. The LWR and SWP spectra are modelled separately using the  $\chi^2$  minimisation technique in XSPEC. To improve the signal-to-noise ratio, we bin the spectra by combining every two adjacent wavelength bins. The size of each bin is 3.35 Å after binning. No interpolation or smoothing is used. Both SWP and LWR spectra are fitted, with combinations of a powerlaw function to represent the continuum and multiple Lorentzian components to describe the emission lines, in the wavelength range of 1180-1800 Å and 1980-3220 Å respectively. The  $\chi^2$  per degrees of freedom is found to be 163.49/163 for SWP05514 and 198.47/164 for LWP01708. Using the best fit model, we fit individual IUE spectra by fixing the continuum powerlaw and letting the other parameters vary. The time-averaged UV spectrum along with the model components and residuals for SWP and LWR are shown in Figure 4 and Figure 5 respectively, and the corresponding best-fit parameters for SWP are listed in Table 2. The goodness of fit is quantified by computing the root mean square (RMS) of

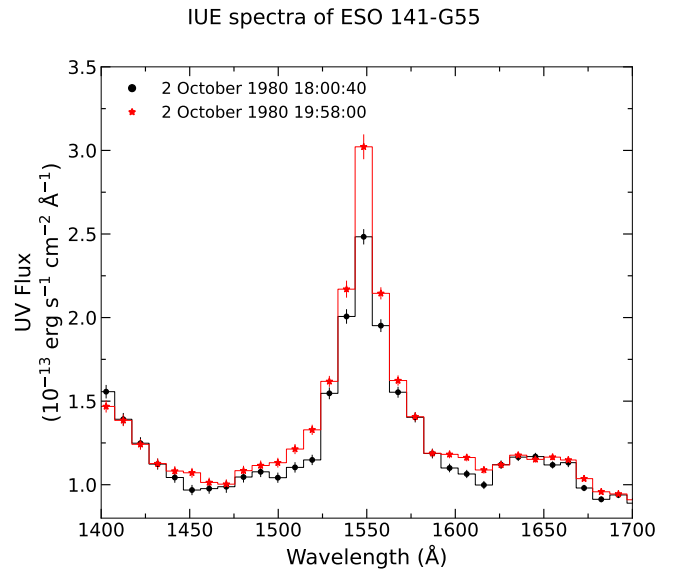


**FIGURE 3** UV variability of ESO 141-G55 as observed on 5 June 1980 at 20:56:49 (circles) and 2 October 1980 at 19:58:00 (stars). IUE spectra in the wavelength range of 1550–1670 Å show a substantial change in the flux level.

the residuals, yielding an RMS value of 0.97 for SWP05514 and 1.09 for LWP01708. Hence the deviations between model and data are consistent with the expected observational uncertainties. The powerlaw energy spectral index from the best-fit

**TABLE 1** IUE data of ESO 141-G55.

Data ID	Observation Start Time (YYYY-MM-DD HH:MM:SS)	Exp Time (s)	Data ID	Observation Start Time (YYYY-MM-DD HH:MM:SS)	Exp Time (s)
SWP05514	1979-06-14 11:14:03	3600	SWP14399	1981-07-05 01:49:39	3000
SWP09200	1980-06-05 20:56:49	3180	SWP15256	1981-10-13 21:39:00	480
SWP10269	1980-10-02 18:00:40	3600	SWP15468	1981-11-09 16:04:19	3600
SWP10270	1980-10-02 19:58:00	4800	SWP16428	1982-02-26 03:06:21	3000
SWP10298	1980-10-07 07:54:51	3000	SWP16560	1982-03-18 00:37:23	3180
SWP10643	1980-11-20 17:51:44	3000	SWP16788	1982-04-18 17:55:30	3900
SWP10644	1980-11-20 19:08:49	2280	SWP17622	1982-08-07 20:08:21	3600
SWP10741	1980-12-03 12:45:30	3600	SWP18095	1982-09-24 15:23:07	1680
SWP13453	1981-03-10 12:39:11	9540	SWP18241	1982-10-08 12:30:45	4500
SWP13454	1981-03-10 17:45:08	5160	SWP18383	1982-10-24 12:47:06	3600
SWP13563	1981-03-24 04:31:22	2700	SWP18455	1982-11-02 12:56:40	3600
SWP13617	1981-03-31 00:36:55	3000	SWP18507	1982-11-08 17:00:23	3000
SWP14275	1981-06-18 03:23:14	3600			
LWR04779	1979-06-14 12:19:20	3600	LWR10890	1981-06-18 04:27:05	4500
LWR08940	1980-10-02 16:55:25	3600	LWR11010	1981-07-05 02:44:15	3780
LWR08941	1980-10-02 19:07:00	2700	LWR11952	1981-11-09 17:08:27	3600
LWR08962	1980-10-07 06:47:38	2400	LWR13043	1982-04-19 16:14:00	5700
LWR09352	1980-11-20 16:56:29	3000	LWP01631	1982-08-07 19:14:48	3000
LWR09425	1980-12-03 11:40:10	3600	LWP01632	1982-08-07 21:12:03	3000
LWR10116	1981-03-10 15:23:03	8280	LWP01708	1982-11-08 16:06:49	3000
LWR10198	1981-03-24 05:20:49	3300			

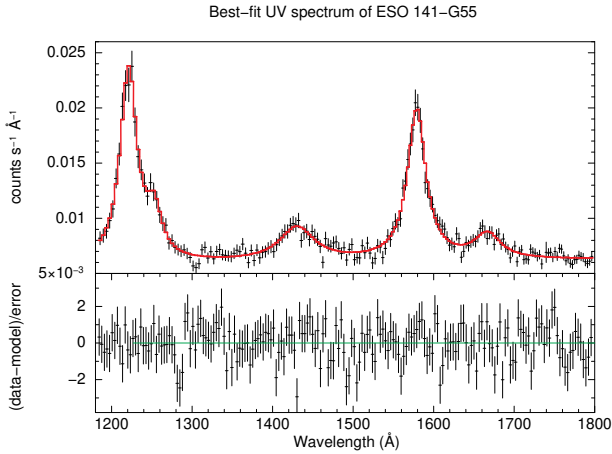


**FIGURE 4** The best-fit SWP UV spectrum (1180-1800 Å) from IUE is shown (top panel) along with the fitted model (red) consisting of continuum and emission features and the residual of the fitting (bottom panel).

average UV spectrum is observed to be  $2.20 \pm 0.16$ , which is consistent with that typically observed from AGN (Pahari et al., 2020; Shull, Stevans, & Danforth, 2012).

Using a convolution model (CFLUX in XSPEC), we derive the continuum-subtracted flux of the peaks of the spectra and

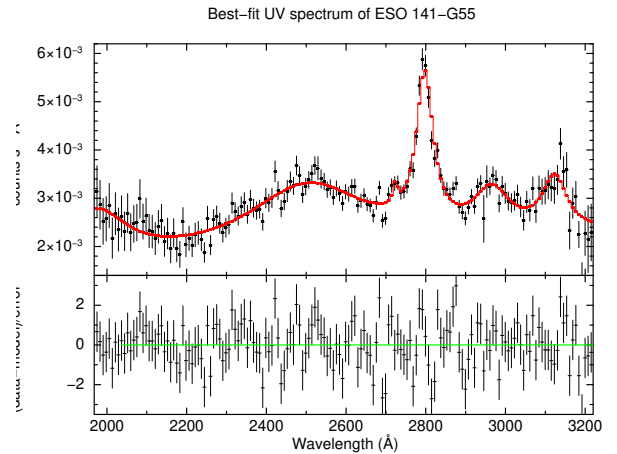


**FIGURE 5** The best-fit LWP UV spectrum (2000- 3200 Å) from IUE is shown (top panel) along with the fitted model (red) consisting of continuum and emission features and the residual of the fitting (bottom panel).

their  $1\sigma$  errors. There is one significant peak in LWR, and the SWP show three peaks. Using the same models, we extract the flux of continuum in the range 2098-2221 Å for LWR and in the ranges 1763-1783 Å and 1356-1376 Å for SWP spectra.

**TABLE 2** Fitted parameters for SWP05514.

Emission line	Component	Parameter	Value
CIV	lorentz	LineE (eV)	$7.73 \pm 0.02$
		Width (eV)	$0.13 \pm 0.01$
		norm	$0.63 \pm 0.15$
SiIV	lorentz	LineE (eV)	$8.53 \pm 0.05$
		Width (eV)	$0.31 \pm 0.01$
		norm	$0.23 \pm 0.11$
Ly $\alpha$	lorentz	LineE (eV)	$9.85 \pm 0.01$
		Width (eV)	$0.17 \pm 0.02$
		norm	$0.58 \pm 0.06$
HeII	lorentz	LineE (eV)	$7.27 \pm 0.01$
		Width (eV)	$0.18 \pm 0.02$
		norm	$0.14 \pm 0.01$
NV	lorentz	LineE (eV)	$9.64 \pm 0.09$
		Width (eV)	$0.14 \pm 0.02$
		norm	$0.12 \pm 0.11$
	powerlaw	PhoIndex	$2.20 \pm 0.16$
		norm	$0.03 \pm 0.01$
$\chi^2/\text{dof}$			163.49/163

## 4 | LIGHTCURVE EXTRACTION AND RESULTS

The ultraviolet light curves of ESO 141-G55, constructed from both the continuum and line fluxes of the spectral observations as a function of time, are presented in Figures 6 and 7. The panels display the temporal variations of both the continuum and the principal emission lines. The continuum fluxes are measured in relatively line-free regions at 1763-1783 Å (CONT1), 1356-1376 Å (CONT2) and 2098-2221 Å (CONT3), while the line fluxes correspond to the CIV (1550 Å), HeII (1650 Å), SiIV (1403 Å) and MgII (2800 Å) emission features. All fluxes are plotted as a function of Modified Julian Date (MJD) and expressed in units of  $10^{-12}$  erg  $\text{s}^{-1}$   $\text{cm}^{-2}$ . The light curves span a total duration of approximately 800 days, with an average cadence (although non-uniform) of  $\sim 40$  days between successive IUE exposures. The flux values are presented in Table 3 and Table 4. In Table 5, we provide the average flux of each continuum and line lightcurves along with their standard deviations (SD). Large SD values for all lightcurves imply the presence of significant variability in both UV line and continuum. The continuum exhibits moderate variability over the monitoring period, with flux changes of about 2040 %, whereas the emission lines show stronger fluctuations, in particular the CIV and SiIV lines, which vary by factors of up to two. There is a correlated trend between the continuum and line lightcurves and to quantify it we have measured the time delay between them.

### 4.1 | Time lag analysis

To measure the reverberation delay between UV continuum and UV lines, we have used JAVELIN. JAVELIN (Zu, Kochanek, Kozłowski, & Peterson, 2016; Zu, Kochanek, Kozłowski, & Udalski, 2013; Zu, Kochanek, & Peterson, 2011) is a widely used tool for estimating time lags between two light curves. It relies on the damped random walk (DRW) model (Kelly, Bechtold, & Siemiginowska, 2009), which characterises light curve variability using a set of parameters including the time lag to simultaneously fit both curves. The parameter distributions are then sampled using the Markov Chain Monte Carlo (MCMC) method, allowing for a probabilistic understanding of the lag and other model parameters. This methodology has been extensively adopted in earlier RM studies.

In this work, we utilise JAVELINs PMAP model. PMAP assumes that the line-band light curve consists of a combination of the continuum signal and a time-delayed emission line component. The model fitting process yields the relative amplitudes of these two components, offering an estimate of the emission line's contribution within the broadband flux. We have used all continuum and line lightcurves for lag analysis as shown in Figure 6. However, due to an insufficient number of data points in lightcurves extracted from LWR spectra (shown in Figure 7), we avoided time lag analysis for LWR data. The model lightcurve flux, along with the uncertainty, is shown in the top panel of Figure 8. We run MCMC for 100000 chains with 500 walkers after burning the first 10000 steps. A frequency distribution of the time delay between the UV continuum and UV line is shown in the middle panel of Figure 8. Lag estimations between two continuum bands and three main UV lines: SiIV, CIV and HeII are provided with 68% errors in Table 6.

In addition to the JAVELIN modeling approach, we also performed an independent cross-correlation analysis using the Interpolated Cross-Correlation Function (ICCF) method (Gaskell & Peterson, 1987; Peterson et al., 1998), which is a widely adopted techniques for reverberation lag estimation. The ICCF provides a non-parametric means of estimating time delays by interpolating between unevenly sampled light curves and computing the cross-correlation coefficient as a function of lag. To calculate uncertainties on ICCF lag, we used Monte-Carlo based Flux Randomization (FR) and Random Subset Selection method (RSS) as outlined by Peterson and et al. (2004); Peterson et al. (1998). Using 10000 MC realisations, we calculate centroid lag distributions for which cross correlation coefficient is 0.8 or higher. The lag distribution is shown in the bottom panel of Figure 8. The ICCF lag with  $1\sigma$  error is found to be  $2.31 \pm 0.83$  days, which is consistent with the JAVELIN estimations (shown in the middle panel of Figure 8).

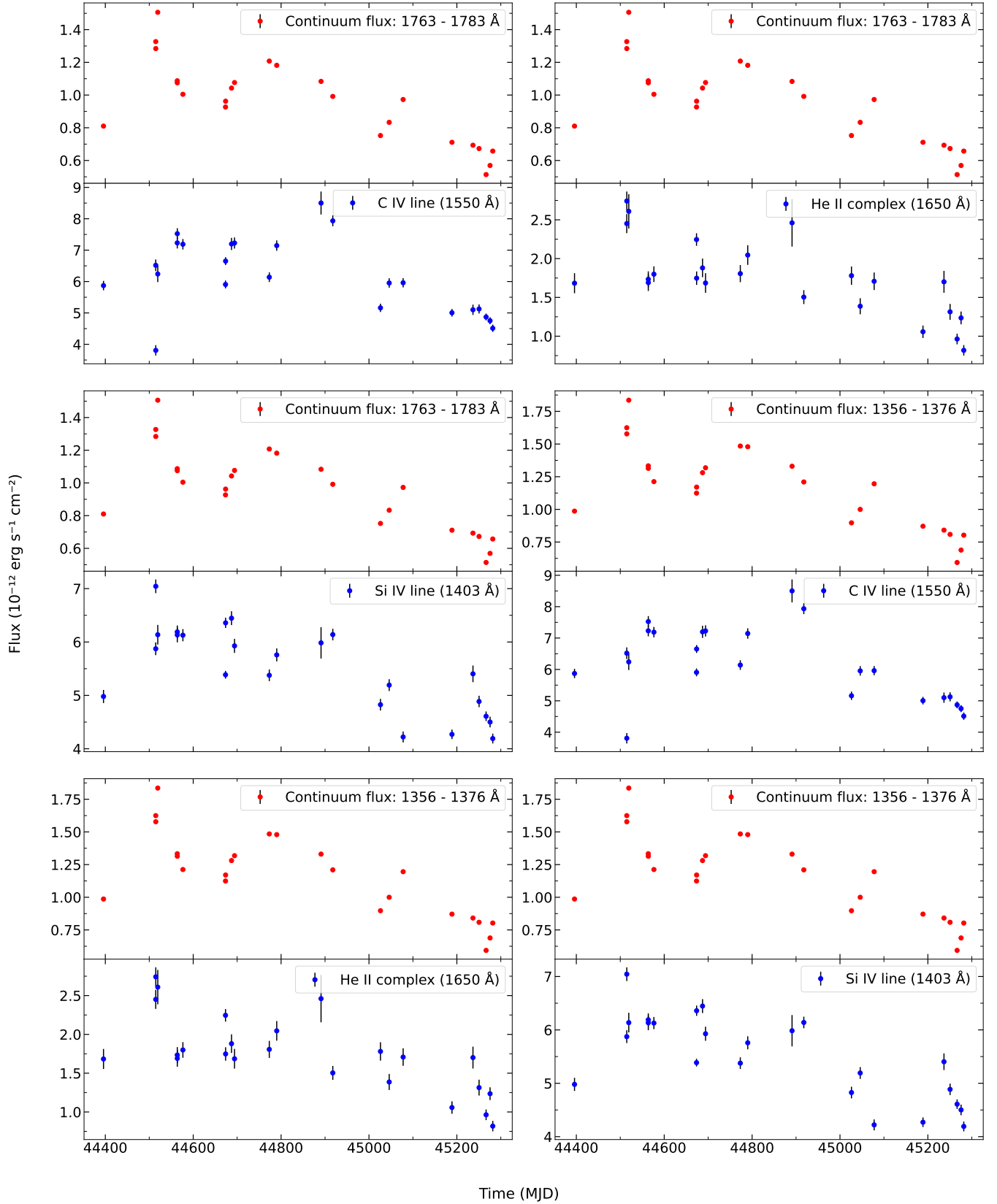


**FIGURE 6** The variation of UV continuum fluxes (in the wavelength range 1356-1376 Å and 1763-1783 Å) for different observations as calculated from fitted UV spectra along with line fluxes for the same observations due to CIV (1550 Å), HeII (1650 Å) and SiIV (1403 Å) lines.

**TABLE 3** Fluxes in the unit of  $10^{-12}$  erg s $^{-1}$  cm $^{-2}$  are provided from SWP spectral modelling. CONT1 and CONT2 are continuum fluxes calculated in the wavelength ranges of 1763-1783 Å and 1356-1376 Å respectively.

Data ID	CONT1 flux	CONT2 flux	C IV flux	He II/O complex flux	Si IV flux
SWP05514	1.11 ± 0.00	1.35 ± 0.01	6.60 ± 0.15	2.54 ± 0.13	6.24 ± 0.12
SWP09200	0.81 ± 0.01	0.99 ± 0.01	5.87 ± 0.15	1.68 ± 0.13	4.98 ± 0.12
SWP10269	1.33 ± 0.01	1.62 ± 0.01	6.52 ± 0.19	2.45 ± 0.12	5.87 ± 0.12
SWP10270	1.28 ± 0.01	1.58 ± 0.01	3.81 ± 0.17	2.74 ± 0.12	7.04 ± 0.13
SWP10298	1.51 ± 0.01	1.84 ± 0.01	6.24 ± 0.26	2.61 ± 0.22	6.14 ± 0.18
SWP10643	1.09 ± 0.01	1.33 ± 0.01	7.23 ± 0.18	1.73 ± 0.10	6.19 ± 0.12
SWP10644	1.07 ± 0.01	1.31 ± 0.01	7.52 ± 0.17	1.69 ± 0.11	6.13 ± 0.14
SWP10741	1.00 ± 0.01	1.21 ± 0.01	7.19 ± 0.17	1.80 ± 0.10	6.13 ± 0.11
SWP13453	0.93 ± 0.01	1.12 ± 0.01	5.91 ± 0.13	2.25 ± 0.08	5.39 ± 0.07
SWP13454	0.96 ± 0.01	1.17 ± 0.01	6.65 ± 0.12	1.75 ± 0.09	6.36 ± 0.10
SWP13563	1.04 ± 0.01	1.28 ± 0.01	7.20 ± 0.19	1.88 ± 0.12	6.45 ± 0.13
SWP13617	1.08 ± 0.01	1.32 ± 0.01	7.23 ± 0.18	1.69 ± 0.13	5.93 ± 0.13
SWP14275	1.21 ± 0.01	1.48 ± 0.01	6.14 ± 0.15	1.81 ± 0.11	5.38 ± 0.11
SWP14399	1.18 ± 0.01	1.48 ± 0.01	7.14 ± 0.17	2.05 ± 0.13	5.76 ± 0.12
SWP15256	1.08 ± 0.01	1.33 ± 0.02	8.50 ± 0.37	2.46 ± 0.31	5.98 ± 0.29
SWP15468	0.99 ± 0.01	1.21 ± 0.01	7.93 ± 0.17	1.50 ± 0.09	6.14 ± 0.11
SWP16428	0.75 ± 0.01	0.90 ± 0.01	5.16 ± 0.13	1.78 ± 0.12	4.83 ± 0.11
SWP16560	0.83 ± 0.01	1.00 ± 0.01	5.95 ± 0.15	1.39 ± 0.10	5.19 ± 0.11
SWP16788	0.97 ± 0.01	1.20 ± 0.01	5.96 ± 0.15	1.71 ± 0.11	4.22 ± 0.10
SWP17622	0.71 ± 0.01	0.87 ± 0.01	5.00 ± 0.12	1.06 ± 0.08	4.27 ± 0.09
SWP18095	0.69 ± 0.01	0.84 ± 0.01	5.10 ± 0.16	1.70 ± 0.14	5.40 ± 0.16
SWP18241	0.67 ± 0.01	0.81 ± 0.01	5.13 ± 0.14	1.31 ± 0.10	4.89 ± 0.11
SWP18383	0.51 ± 0.01	0.59 ± 0.01	4.87 ± 0.11	0.96 ± 0.07	4.61 ± 0.09
SWP18455	0.57 ± 0.01	0.69 ± 0.01	4.75 ± 0.11	1.24 ± 0.08	4.50 ± 0.10
SWP18507	0.66 ± 0.01	0.80 ± 0.01	4.51 ± 0.12	0.82 ± 0.07	4.19 ± 0.09

As an independent cross-check on the ICCF and JAVELIN results, we also estimated the time delay using the z-transformed discrete correlation function (ZDCF; (Alexander, 1997)), which is designed for unevenly sampled light curves and employs equal-population binning to mitigate biases arising from sparse or irregular cadence. The ZDCF was computed using data-driven lag bins containing a minimum number of pairs, and uncertainties were estimated via a flux-randomisation and random-subset-selection (FR/RSS) Monte Carlo procedure similar to that adopted in ICCF analyses. From the resulting ZDCF correlation function, the lag was determined from the peak of the correlation distribution. This analysis yields a time delay of  $3.57 \pm 1.88$  days between the 1356–1376 Å UV continuum and the 1550 Å C IV emission-line light curve, in good agreement with the corresponding lag reported in Table 6. While this delay lies near the practical detectability limit imposed by the sampling, its consistent recovery across the ZDCF, ICCF, and JAVELIN analyses suggests a short reverberation timescale, although its proximity to the cadence warrants cautious interpretation.

The limitations imposed by the temporal sampling are particularly relevant for the lag measurements obtained using both the ICCF and JAVELIN analyses presented in Section 4.1. In the ICCF method, the effective sensitivity to a given lag is governed by the distribution of time separations between paired continuum and line measurements that enter the flux-randomization and random subset selection (FR/RSS) realizations, rather than by the median cadence alone (Peterson & et al., 2004; Peterson et al., 1998). Although the median sampling interval of the IUE light curves is  $\Delta t_{\text{med}} \sim 10 - 15$  days, the presence of several clusters of closely spaced observations (Table 1) provides a limited number of correlation pairs at delays of a few days, allowing the ICCF centroid distribution (bottom panel of Figure 5) to weakly probe short lags. In the JAVELIN analysis, the continuum variability is modeled as a damped random walk and the emission-line light curve is forward-modeled using the PMAP formalism; while this approach can interpolate between unevenly sampled epochs, its ability to constrain lags significantly shorter than  $\Delta t_{\text{med}}$  remains dependent on the availability of short-spacing data

**TABLE 4** Fluxes in the unit of  $10^{-12}$  erg  $s^{-1}$   $cm^{-2}$  are provided from LWP spectral modelling. CONT3 is the continuum flux calculated in the wavelength ranges of 2098–2221 Å.

Data ID	CONT3 flux	Mg II flux
LWR04779	$2.31 \pm 0.03$	$1.64 \pm 0.10$
LWR08940	$2.48 \pm 0.03$	$1.24 \pm 0.10$
LWR08941	$3.41 \pm 0.04$	$1.52 \pm 0.10$
LWR08962	$2.76 \pm 0.05$	$1.52 \pm 0.15$
LWR09352	$2.39 \pm 0.03$	$1.74 \pm 0.12$
LWR09425	$1.62 \pm 0.03$	$2.60 \pm 0.12$
LWR10116	$3.30 \pm 0.03$	$1.30 \pm 0.07$
LWR10198	$2.85 \pm 0.03$	$1.10 \pm 0.09$
LWR10890	$2.92 \pm 0.03$	$0.71 \pm 0.08$
LWR11010	$2.82 \pm 0.03$	$2.12 \pm 0.10$
LWR11952	$2.80 \pm 0.03$	$1.46 \pm 0.08$
LWR13043	$1.96 \pm 0.03$	$0.66 \pm 0.08$
LWP01631	$2.34 \pm 0.02$	$1.55 \pm 0.05$
LWP01632	$2.29 \pm 0.02$	$1.62 \pm 0.05$
LWP01708	$2.21 \pm 0.02$	$1.15 \pm 0.04$

**TABLE 5** Weighted mean flux (in unit of  $10^{-12}$  erg  $s^{-1}$   $cm^{-2}$ ) and standard deviation of continuum and emission lines.

Lightcurve type	Mean Flux	Standard Deviation
CONT1	$0.91 \pm 0.001$	$24 \pm 04$ %
CONT2	$1.10 \pm 0.001$	$31 \pm 05$ %
CONT3	$2.46 \pm 0.006$	$42 \pm 10$ %
C IV	$5.82 \pm 0.03$	$107 \pm 17$ %
He II	$1.56 \pm 0.02$	$49 \pm 08$ %
Si IV	$5.33 \pm 0.02$	$79 \pm 13$ %
Mg II	$1.39 \pm 0.02$	$43 \pm 11$ %

and on the assumed stochastic variability model (Zu et al., 2011). Consequently, lag estimation to calculate uncertainties on ICCF lag, we used Monte-Carlo-based Flux Randomisation (FR) and Random Subset Selection method (RSS) as outlined by Peterson and et al. (2004); Peterson et al. (1998). Earlier model dependence than longer delays. We accordingly interpret these short-lag measurements as tentative, while noting their consistency between the two independent methods.

## 5 | DISCUSSION

We have analysed IUE ultraviolet spectra for ESO 141–G55, which shows substantial variability in both UV continuum and emission lines. Our time lag analysis of the emission lines with

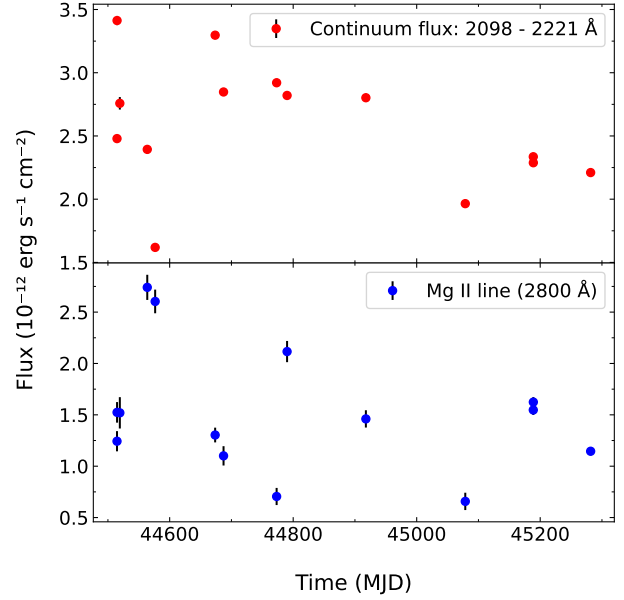


**FIGURE 7** Top panel shows the variation of UV continuum fluxes (in the wavelength range 2098–2221 Å) for different observations as calculated from fitted UV spectra. Bottom panel shows the line flux for the same observations due to the Mg II line at 2800 Å.

**TABLE 6** Estimated Time lag (in days) between UV continuum and UV line variabilities from ESO 141–G55 using damped random walk lightcurve modelling. Errors are calculated using MCMC with 68% confidence.

UV Continuum (wavelength Å)	UV Line (wavelength Å)	Lag (days)
1356–1376 Å	1403 Å	$2.92^{+0.54}_{-0.61}$
1356–1376 Å	1550 Å	$4.41^{+0.44}_{-0.54}$
1356–1376 Å	1650 Å	$4.11^{+0.35}_{-0.81}$
1763–1783 Å	1403 Å	$2.78^{+0.53}_{-0.52}$
1763–1783 Å	1550 Å	$4.48^{+0.45}_{-0.58}$
1763–1783 Å	1650 Å	$4.16^{+0.39}_{-0.46}$

respect to the continuum suggests that the lines are possibly emitting from the inner part of BLR which is close to the accretion disk. The following subsection discusses the evidence supporting this hypothesis.

### 5.1 | Origin of UV line emissions

Our reverberation lag analysis suggests that UV lines like C IV at 1550 Å are delayed to the UV continuum emission by  $\sim 4.41$  light days. Such a time scale roughly corresponds to a

length scale of 0.004 pc or 4 mpc. Therefore, UV lines may be reprocessed from the outer accretion disk.

To explore further, we have calculated line velocities. From Table 2, using best-fit spectra, the FWHM of C<sup>IV</sup> line at  $7.73 \pm 0.02$  eV is  $0.126 \pm 0.003$  eV. This corresponds to the line width of 26.5 Å. The velocity width, due to Doppler broadening, will be  $\Delta v = \frac{\Delta\lambda}{\lambda} \cdot c = 4965 \pm 311$  km/s. Such a broadening is consistent with the BLR origin of UV lines as suggested by Mandal et al. (2021). When similar exercise is applied by the Si<sup>IV</sup> line, using the best-fit values from Table 2, we get line width of  $0.314 \pm 0.013$  eV for the line energy  $8.53 \pm 0.05$  eV. This corresponds to the velocity width of  $11031 \pm 677$  km/s. The large velocity width of the Si<sup>IV</sup> component is naturally consistent with emission from the inner BLR region. Si<sup>IV</sup> is a high-ionization line and is expected to arise at smaller radii than low-ionization species, where the gravitational potential of the central supermassive black hole dominates the gas dynamics. For ESO 141-G55, a well-studied unobscured Seyfert 1 galaxy with a strong UV/X-ray ionizing continuum, such velocities maybe compatible with virialized gas located at light-day scales. The absence of strong obscuration and the known presence of a classical BLR in this source favor an origin in the inner BLR, where high-ionization species can attain large Doppler widths through Keplerian motion. An alternative interpretation is that the broad Si<sup>IV</sup> component traces a radiatively driven disk wind launched from the inner accretion disk. High-ionization UV lines such as Si<sup>IV</sup> are particularly sensitive to outflowing gas exposed to the intense EUV and soft X-ray radiation field. In ESO 141-G55, which shows evidence for ionized outflows in X-ray spectra with a speed of  $\sim 0.17c$  (Porquet et al., 2024), the broad velocity width can be explained by a combination of rotational motion at the wind base and radial acceleration along the flow. Such disk winds are expected to originate at radii comparable to or interior to the classical BLR, naturally producing line widths of order  $10^4$  km s<sup>-1</sup>. This hypothesis is consistent with our UV line lag measurements. Si<sup>IV</sup> is delayed by  $2.92^{+0.54}_{-0.61}$  days with respect to UV continuum, which is significantly shorter than C<sup>IV</sup> line lag, which is  $4.41^{+0.44}_{-0.54}$  days. Therefore, measured lag suggests that the observed Si<sup>IV</sup> emission probes the dynamical interface between the inner BLR and an accretion-disk-driven outflow.

From the best-fit spectrum, we have computed 1450 Å flux (by integrating the flux in the range of 1440–1460 Å) and average fluxes for all observations provided in Table 1. The average 1450 Å flux is found to be  $1.19 \pm 0.03 \times 10^{-12}$  ergs s<sup>-1</sup> cm<sup>-2</sup>. Using the luminosity distance of 163.6 Mpc to ESO 141-G55 (Collaboration et al., 2020; Wright, 2006), we have computed the continuum UV luminosity at 1450 Å which is  $3.9 \pm 0.11 \times 10^{42}$  ergs s<sup>-1</sup>. Comparing the 1450 Å luminosity with the scaling relation from Kaspi et al. (2005), we noted that the

BLR size is approximately 4.5 days. This is consistent with the lag between UV lines and continuum measured directly by cross-correlating UV continuum and line lightcurves in our work. Further multi-wavelength studies of the source will be potentially useful to understand the BLR structure close to the accretion disk.

## 6 | CONCLUSIONS

A detailed ultraviolet spectroscopic investigation of the Seyfert 1 galaxy ESO 141-G55 is carried out using archival data from the International Ultraviolet Explorer (IUE) obtained over multiple epochs between 1978 and 1982. The analysis reveals prominent UV emission lines, including Si<sup>IV</sup>, C<sup>IV</sup>, and HeII, arising from ionised gas in the broad-line region (BLR). These features exhibit significant variability and are found to lag behind the UV continuum emission by 2.92, 4.41, and 4.11 light days, respectively. These values correspond to a distance of  $\sim 0.004$  pc, suggesting that the UV line-emitting regions are located in the inner parts of the BLR, close to the accretion disk. The observed line widths imply high-velocity motions, consistent with Doppler broadening expected from dynamic BLR clouds. The UV continuum luminosity at 1450 Å, combined with empirical size-luminosity scaling relations, further supports a BLR size of  $\sim 4.5$  light days, which is in agreement with our lag measurements. For a better understanding of the structure and physical conditions of this region, additional high-cadence, multiwavelength observations will be essential.

## ACKNOWLEDGMENTS

We thank the referee for constructive comments which help to improve the manuscript. MP acknowledges the research facility used at the Department of Physics, IIT Hyderabad.

## REFERENCES

- Alexander, T. (1997, January), Is AGN Variability Correlated with Other AGN Properties? ZDCF Analysis of Small Samples of Sparse Light Curves. In D. Maoz, A. Sternberg, & E. M. Leibowitz (Eds.), *Astronomical Time Series Vol. 218*, p. 163. doi:
- Ayres, T. R. (1993), *Publications of the Astronomical Society of the Pacific*, 105(687), 538.
- Blandford, R. D., & McKee, C. F. (1982), *ApJ*, 255, 419–439.
- Cackett, E. M., Gelbord, J., Barth, A. J. et al. (2023, December), *ApJ*, 958(2), 195. doi:
- Cackett, E. M., Horne, K., & Winkler, H. (2007), *Monthly Notices of the Royal Astronomical Society*, 380(2), 669–682.
- Calzetti, D. (1999, March), *Ap&SS*, 266, 243-253.
- Chapman, J. M., & et al. (1985), *ApJ*, 297, 151.
- Clavel, J., et al. (1991), *ApJ*, 366, 64.

- Collaboration, P., et al. (2020), *Astronomy and Astrophysics*, 641, A7.
- Collier, S., & et al. (1999), *MNRAS*, 302, L24.
- Edelson, R. A., & Krolik, J. H. (1988, October), *ApJ*, 333, 646. doi:
- Elvis, M., & et al. (1978), *MNRAS*, 183, 129.
- Fausnaugh, M. M., Denney, K. D., Barth, A. J. et al. (2016, April), *ApJ*, 821(1), 56. doi:
- Gaskell, C. M., & et al. (1981), *IAU Circ.*, 3560, 1.
- Gaskell, C. M., & Peterson, B. M. (1987, September), *ApJS*, 65, 1. doi:
- Grupe, D., & Mathur, S. (2004), *Nuclear Physics B - Proceedings Supplements*, 132, 185.
- Guo, H., Barth, A. J., & Wang, S. (2022, November), *ApJ*, 940(1), 20. doi:
- Kaspi, S., Maoz, D., Netzer, H., Peterson, B. M., Vestergaard, M., & Jannuzi, B. T. (2005), *The Astrophysical Journal*, 629(1), 61.
- Kelly, B. C., Bechtold, J., & Siemiginowska, A. (2009, June), *ApJ*, 698(1), 895-910. doi:
- Khachikian, E. Y., & Weedman, D. W. (1974), *ApJ*, 192, 581-589.
- Koratkar, A., & Gaskell, C. M. (1991), *ApJS*, 75, 719.
- Mandal, A. K., Rakshit, S., Stalin, C. S., Petrov, R. G., Mathew, B., & Sagar, R. (2021, April), *MNRAS*, 502(2), 2140-2157. doi:
- Nichols, J., Garhart, M., De La Pena, M., & Levay, K. (1993), IUE NEWSIPS Image Processing System Information Manual: Low Dispersion Data. Version.
- Osterbrock, D. E. (1981), *ApJ*, 249, 462-470.
- Pahari, M., McHardy, I. M., Vincentelli, F. et al. (2020), *Monthly Notices of the Royal Astronomical Society*, 494(3), 4057-4068.
- Peterson, B. M. (1993), *PASP*, 105, 247.
- Peterson, B. M., & et al. (2004), *ApJ*, 613, 682.
- Peterson, B. M., Wanders, I., Horne, K., Collier, S., Alexander, T., Kaspi, S., & Maoz, D. (1998, June), *PASP*, 110(748), 660-670. doi:
- Porquet, D., Reeves, J. N., Hagen, S., Lobban, A., Braitto, V., Grosso, N., & Marin, F. (2024), *Astronomy & Astrophysics*, 689, A336.
- Shakura, N. I., & Sunyaev, R. A. (1973), *A&A*, 24, 337-355.
- Shull, J. M., Stevans, M., & Danforth, C. W. (2012), *The Astrophysical Journal*, 752(2), 162.
- Turner, T. J., & et al. (1991), *ApJS*, 75, 561.
- Turner, T. J., & et al. (1993), *ApJ*, 407, 556.
- Turner, T. J., & Pounds, K. A. (1989), *MNRAS*, 240, 833.
- Vaucouleurs, G., Vaucouleurs, A., Corwin, H. G., Buta, R. J., Paturel, G., & Fouqué, P. 1991, *Third Reference Catalogue of Bright Galaxies: Volume II*. Springer.
- Wanders, I., Peterson, B. M., Alloin, D. et al. (1997), *The Astrophysical Journal Supplement Series*, 113(1), 69.
- Ward, M., & et al. (1978), *ApJ*, 223, 788.
- Ward, M. J., Penston, M. V., Blades, J. C., & Turtle, A. J. (1978), *Astrophysical Journal*, 223, 788-796.
- Wright, E. L. (2006, December), *PASP*, 118(850), 1711-1715. doi:
- Zu, Y., Kochanek, C. S., Kozłowski, S., & Peterson, B. M. (2016, March), *ApJ*, 819(2), 122. doi:
- Zu, Y., Kochanek, C. S., Kozłowski, S., & Udalski, A. (2013, March), *ApJ*, 765(2), 106. doi:
- Zu, Y., Kochanek, C. S., & Peterson, B. M. (2011, July), *ApJ*, 735(2), 80. doi:

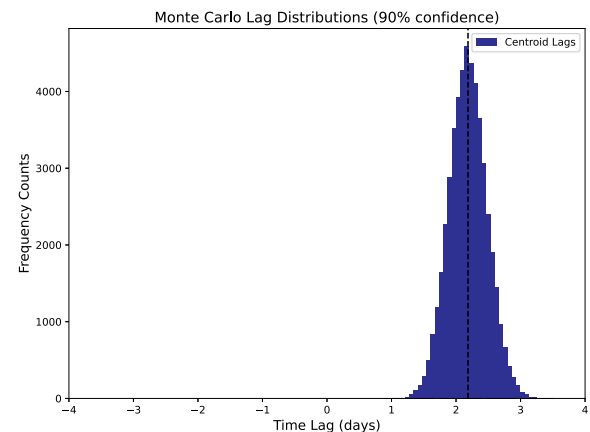
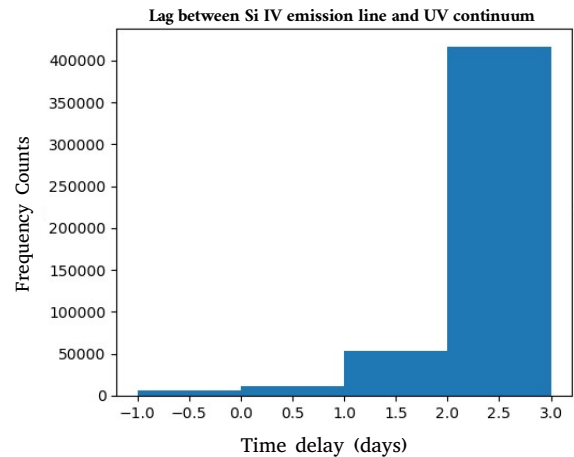
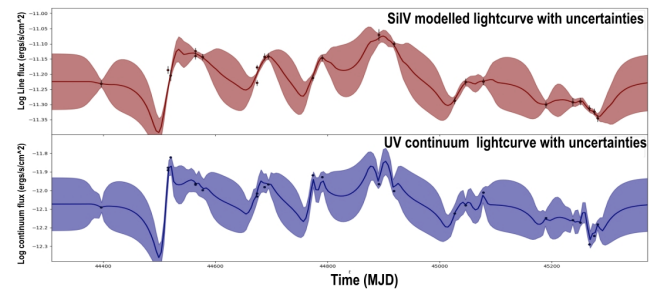


**FIGURE 8** Top panel shows Lightcurves due to SiIV line fluxes (top) and UV continuum fluxes at 1356-1376 Å (bottom), along with fitted PMAP reverberation model and 68% uncertainty. The middle panel shows the posterior distribution of time delay between the above two lightcurves derived through MCMC simulations. Bottom panel shows the distribution of time delays estimated by ICCF method. Uncertainties on ICCF time delays were estimated using the Flux Randomization/Random Subset Selection (FR/RSS) method with 10000 MC realisation.

